

Quantum optics of single electrons in quantum liquid and solid helium-4

Matthew Otten,¹ Xianjing Zhou,¹ Xufeng Zhang,¹ and Dafei Jin^{1,*}

¹Center for Nanoscale Materials, Argonne National Laboratory, Argonne, Illinois 60439, USA

(Dated: June 26, 2019)

Single electrons can be conceived as the simplest quantum nodes in a quantum network. Between electrons, single photons can act as quantum channels to exchange quantum information. Despite this appealing picture, in conventional materials, it is extremely difficult to make individual electrons and photons coherently interact with each other at the visible-infrared wavelengths suitable for long-distance communication. Here we theoretically demonstrate that the self-confined single-electron structure in condensed helium-4 can be a fascinating candidate for single-electron quantum nodes. Each electron in helium forms a bubble of 1 to 2 nm radius and coherently interacts with mid-infrared photons. A parametrically amplified femtosecond laser can drive the electrons into any superposition between the ground and excited states. An electron inside a slot-waveguide cavity can strongly couple with cavity photons and exhibits vacuum Rabi oscillations. Two electrons in the cavity naturally generate entanglement through their respective coupling to the lossy cavity. The electron-in-helium system offers unique insight in understanding nonequilibrium quantum dynamics.

A quantum network consists of quantum nodes and quantum channels [1]. Quantum channels achieve remote quantum information exchange through the universal “flying” qubits — photons [2, 3], whereas quantum nodes perform local quantum information processing via various “trapped” qubits — ions, atoms, molecules, defect centers, quantum dots, *etc.* [4–9]. Beyond these, perhaps the most exotic but simplest quantum node conceivable is a single electron [10, 11]. Unfortunately, single electrons in free space or semiconductor junctions do not resonantly interact with visible-infrared (Vis-IR) photons, and cannot be directly linked to long-distance quantum communication [2, 3].

Here we propose a single-electron quantum-node platform, based on an extraordinary electronic structure in condensed, quantum liquid and solid helium-4 (He-4). An excess electron injected into He-4 spontaneously forms a 1-2 nm radius self-confined structure, called an electron bubble [12–15], which resembles the textbook example of a quantum particle confined in a finite-depth spherical well. The electron can resonantly interact with mid-infrared (mid-IR) photons and the wavelength can be tuned by changing the ambient pressure [16–19]. We find that a femtosecond laser extended into the mid-IR regime by an optical parametric amplifier (OPA) can drive the electron into Rabi oscillations and prepare its wavefunction into arbitrary superpositions between the ground and excited states. A single electron situated inside an on-chip slot-waveguide cavity can strongly couple with cavity photons and exhibit vacuum Rabi oscillations with microseconds lifetime. Two electrons placed in the cavity automatically generate entanglement with each other through their coupling to the lossy cavity. Depending on cavity’s photon loss rate, the entangled states show varied population and concurrence. The electron-in-helium system opens new opportunities for studying coherent nonequilibrium quantum dynamics of a quantum particle embedded in quantum matter [20].

Condensed helium-4 and electron bubble

Liquid and solid He-4 are the purest condensed matter in nature. Crossing the famous λ -transition at about 2 K temperature (depending on the pressure), condensed He-4 changes from a classical matter to a quantum matter [21, 22], as shown in Fig. 1a. In the quantum regime, He-4 takes a quantum liquid-II (superfluid) phase below about 25 bar and a quantum solid phase above [21, 23].

When an excess electron is injected into liquid or solid He-4, it repels the surrounding helium atoms away under the Pauli exclusion and forms a three-dimensional (3D) nanometric quantum well that confines its own wavefunction inside. This structure, as illustrated in Fig. 1b, is called an electron bubble. The characteristic radius of the electron bubble is about 2 nm at zero pressure in the liquid phase. It can be continuously squeezed down to about 1 nm at 50 bar pressure in the solid phase. Since the bubble size is much larger than He-4 atomic size (~ 0.31 Å), the ground-state electron bubble, either in liquid or solid He-4, is almost perfectly spherical [14]. The crystal order of solid He-4 does not affect the electronic and optical properties of electron bubble, except for the size and mobility [16, 17, 24, 25]. In our present study, we include both liquid and solid He-4, focusing on the near-zero temperature $T < 1$ K and liquid-solid transition pressure $p \approx 25$ bar for most calculations.

Electronic structure and optical transitions

The electron confined inside the bubble is an extremely quantum object. It bears a finite potential barrier from the condensed helium,

$$U(p) = \frac{2\pi\hbar^2 l}{m_e} n_{\text{He}}(p), \quad (1)$$

where $l \approx 1$ Å is the s-wave scattering length between an electron and a helium atom, n_{He} is the bulk helium number density as a function of pressure, and U is the

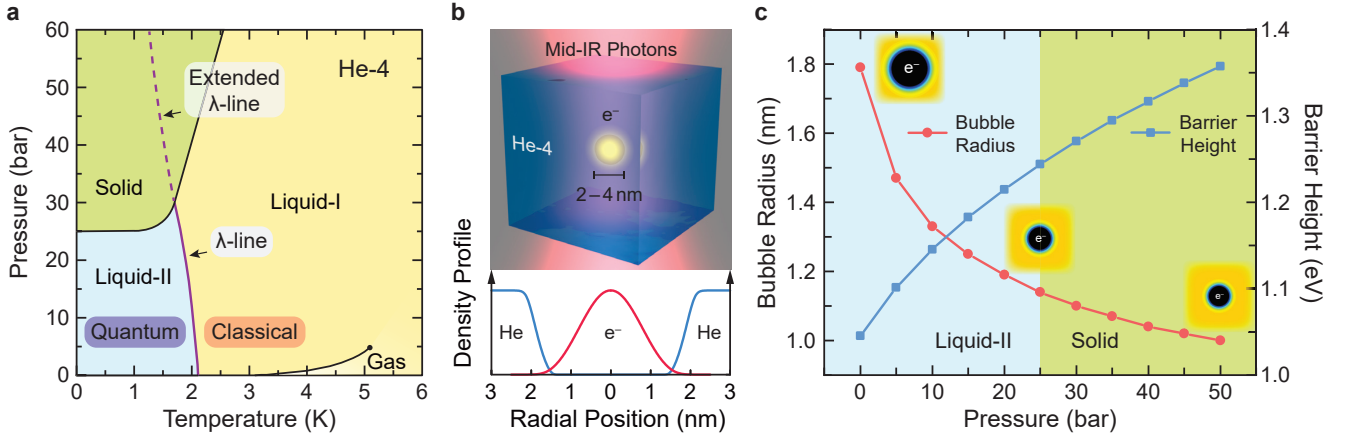


Fig. 1. Self-confinement of a single electron in condensed He-4. **a.** Phase diagram of He-4. The λ -line (and its extension) separates the quantum and classical matter regimes in both the liquid and solid phases. **b.** Upper panel: Schematics of a spherical ground-state electron bubble under optical exposure of mid-infrared (mid-IR) photons. The diameter of the bubble is tunable between 2 to 4 nm under 0 to 50 bar pressure. Lower panel: Density-functional calculated helium and electron density profile at zero pressure. **c.** Ground-state bubble radius R and potential barrier height U from the bulk He-4 versus pressure at near-zero temperature. The insets display the color plots of calculated helium density around the bubble at 0, 25, and 50 bar pressure.

barrier height, which increases from about 1 to 1.4 eV above the vacuum level as the pressure increases from 0 to 50 bar [26–28]. This barrier is sufficient to generate a series of electron bound states labeled by the angular quantum number $l = 0, 1, 2, \dots$ corresponding to the S, P, D, ... orbitals, and the radial quantum number $n = 1, 2, 3, \dots$ representing the number of nodes in the radial wavefunction [18]. Such electronic structure is the same as that of the textbook example of a quantum particle confined in a finite-depth spherical well [29]. The only difference is that the potential well here is deformable, since the electron and helium make up a self-adjusting system and the interface results from the force balance between electron’s quantum pressure and helium’s hydrodynamic pressure. The interfacial thickness between the electron and helium is of the order of superfluid healing length $\xi \approx 1 \text{ \AA}$. In Fig. 1c, we give the bubble radius R and barrier height U from our density-functional theory (DFT) calculation (see Methods) [19, 28], which has been attested to agree well with experiments. The inset gives the color plot of helium density, which smoothly varies from 0 in the bubble center to n_{He} in the bulk helium. The bubble radius is defined at the position of $\frac{1}{2}n_{\text{He}}$.

Under illumination, the electron in the bubble can transition from the 1S ground state to many excited states. The most relevant transitions are the 1-photon 1S-to-1P, 1-photon 1P-to-2S, and 2-photon 1S-to-2S transitions. Other transitions have much smaller probabilities and can be safely ignored [30]. Figure 2a shows the DFT calculated eigenenergies versus pressure for the representative eigenstates 1S, 1P, and 2S. The typical eigenenergies are of the order of several 100 meV. Figure 2b shows the optical transition wavelengths, which

are in the mid-infrared (mid-IR) regime from 3 to 12 μm . For photon energy exceeding 1 eV, the electron can be ejected via the photoelectric effect into the continuum states of bulk helium, as indicated in Fig. 2a.

Laser-driven Rabi oscillations

Previous studies of optical transitions of electron bubbles were limited to weak and continuous light illumination [16, 17, 31]. The transition probabilities were so low that on average only a small fraction of electrons could end in the excited states. Today’s Ti:Sapphire femtosecond lasers equipped with an OPA and difference frequency generation (DFG) can output several microJoules of pulse energy in mid-IR, with 100 to 200 fs pulse width at 1 to 5 kHz repetition rate [32]. This enables coherently driving an electron in the bubble into Rabi oscillations by each laser pulse [33].

Let us take the pressure $p = 25$ bar. The calculated bubble radius is $R = 1.14$ nm, the 1-photon 1S-to-1P transition wavelength is $\lambda = 5.44 \mu\text{m}$, and electric dipole moment is $d = 0.40$ e-nm. The output pulse energy from an OPA at this wavelength can be as high as 5 μJ [32]. To emulate a realistic experiment, we assume only 10% photons can reach the center of helium cell after multiple reflection on the cryostat windows. This number of photons can be focused into a 100 μm diameter area by a silicon lens. The electric field at the center can be as strong as $\mathcal{E} \approx 0.1 \text{ V nm}^{-1}$, more than enough to produce a few cycles of Rabi oscillations in sub-picoseconds.

Figure 3a-c shows our calculated electron Rabi oscillations between the 1S and 1P states under various laser pulse configurations (see Methods). Fig. 3a has a pulse width $\mathcal{W} = 100$ fs and field strength $\mathcal{E} = 0.1 \text{ V nm}^{-1}$. After one and a quarter cycle, the electron ends up in the 1P state. Fig. 3b has a slightly higher

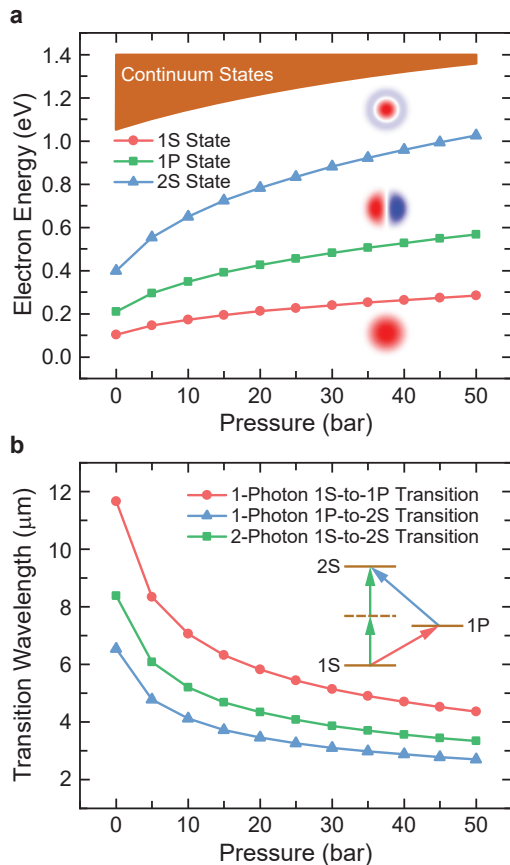


Fig. 2. Electronic and optical structures of a spherical electron bubble. **a.** Eigenenergies and wavefunction profiles of several representative bound states: 1S, 1P and 2S, and the continuum of extended states when the electron is ejected out of the bubble. **b.** Representative optical transition wavelengths between 1S, 1P and 2S states. The inset illustrates the processes.

field strength and doubled pulse width $\mathcal{W} = 200$ fs. After three cycles, the electron is brought back to the 1S state. Importantly, the pulse strength can be tuned to fit an arbitrary superposition of 1S and 1P. Fig. 3c has a pulse width $\mathcal{W} = 200$ fs and a fine-tuned field strength $\mathcal{E} = 0.0085$ V nm $^{-1}$, leaving the electron in an equal superposition of the 1S and 1P states.

The Rabi oscillations are much faster than the spontaneous emission in this system. The latter takes place in microsecond time scale and is thus irrelevant to the optical transitions during a single laser pulse. Nevertheless, interesting phenomena happen after each laser pulse — the bubble shape can deform [18, 19, 34]. This is fundamentally different from the textbook problem of a rigid spherical well. Since the excited electron wavefunction contains nodal surfaces, it breaks the force balance between the electron quantum pressure and helium hydrodynamic pressure. Helium can run into the nodal regions and redefine the electron’s Hamiltonian. This process is often accompanied with

intense phonon emission [19, 34]. Due to the heavy helium atom mass compared with the electron mass (7296 : 1), the characteristic time of shape deformation is 1-10 ps in the liquid phase (varying with pressure) and about 1-10 ns in the solid phase [14, 19]. The latter is 10^3 slower because the mass transport in solid He-4 is by atomic hopping [24, 25]. In any case, the shape deformation is much slower than the laser pulse width. Therefore, during each pulse, the Frank-Condon principle ensures a fixed helium profile and electronic eigenstates, but after the pulse (and before the next pulse arrives in ~ 1 ms), the electron bubble can undergo various intermediate processes until it finally relaxes back to the original 1S ground state.

Figure 3d illustrates several representative intermediate bubble states corresponding to Fig. 3a-c. In the middle, the electron returns to the 1S ground state and the bubble remains spherical. No deformation happens. On the left, the electron ends in the 1P excited state, where the quantum pressure vanishes at the nodal surface. Helium can run into the bubble waist and generate a double-well potential to confine two separated one-half electron wavefunctions with antisymmetric parity. This is known as the unstable fission state of the electron bubble [18, 19, 34, 35]. This process takes several picoseconds in liquid and a few nanoseconds in solid. However, whether this truly happens and how the electron wavefunction loses its coherence have been open questions for years [31, 35–38].

An even more attractive configuration is shown on the right of Fig. 3d. The electron ends in an equal superposition of 1S and 1P states,

$$|1S1P\rangle = \frac{1}{\sqrt{2}} (e^{i\theta_1} e^{-i\omega_{1S}t} |1S\rangle + e^{i\theta_2} e^{-i\omega_{1P}t} |1P\rangle), \quad (2)$$

where θ_1 and θ_2 are initial phases. Due to the presence of a 1S component, the total wavefunction no longer has a stationary nodal surface. The bubble adiabatically evolves into a prolate spheroid shape, which is a long-lived metastable state. The new electronic eigenstates in the bubble are the prolate 1S and 1P states. Later, we shall note that this 1S1P state is related to the dressed states of electron and photons inside a cavity. In the microsecond time scale, the 1P component vanishes by spontaneous radiation and the system returns to the original 1S spherical bubble state.

Figure 3 has only demonstrated several examples. By adjusting the pulse energy in experiment, one can in principle bring the electron into arbitrary superpositions of 1S and 1P states or other high-lying states. This can lead to a variety of bubble shapes together with a variety of quantum dynamics. These extraordinary behaviors suggest that one can use photons to tailor the Hamiltonian and engineer electron wavefunctions in quantum matter He-4. To our knowledge, no other systems share similar capabilities.

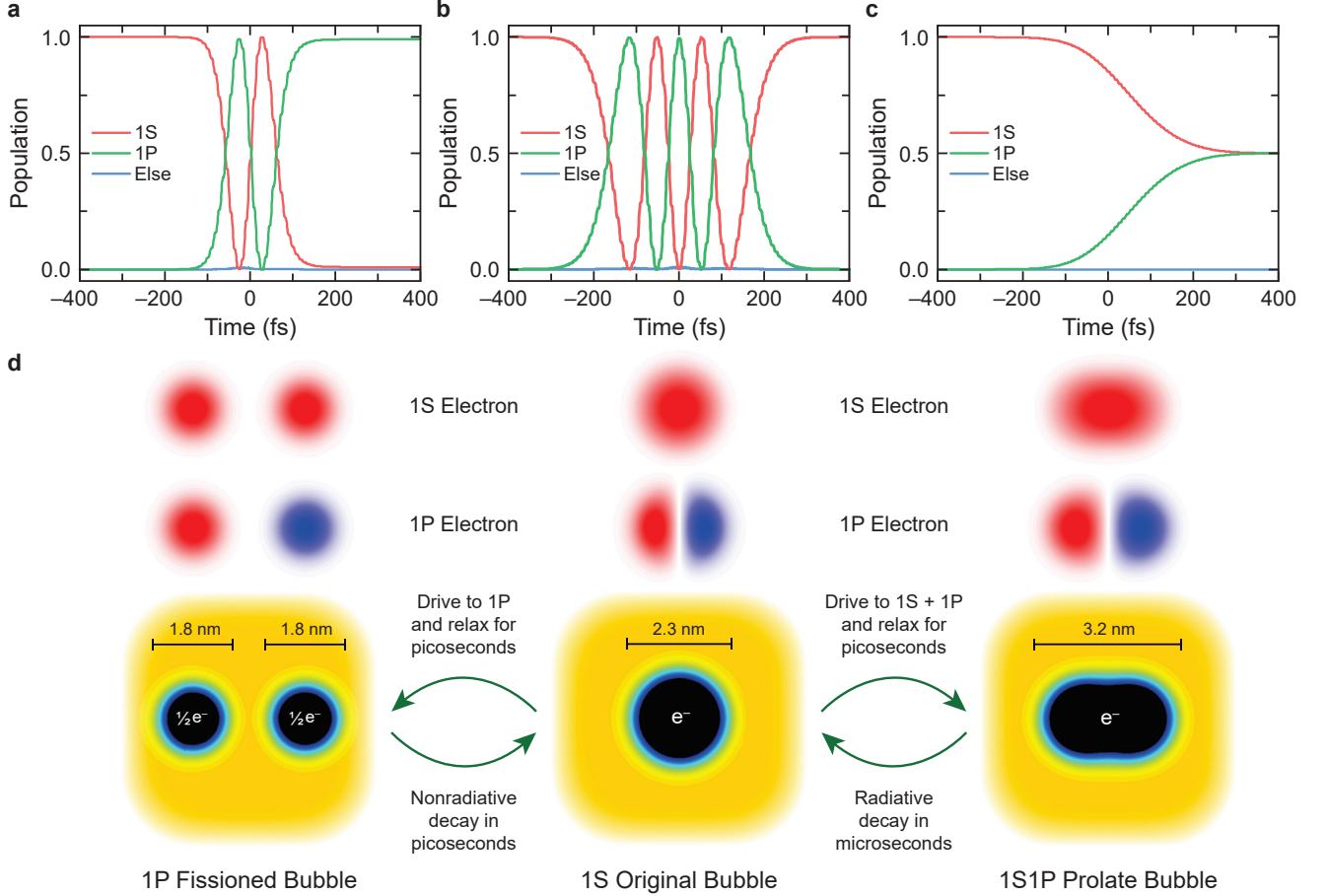


Fig. 3. Laser-driven Rabi oscillations of a single electron in a spherical bubble between 1S and 1P states and the resulting bubble dynamics. **a.** Laser pulse width $\mathcal{W} = 100$ fs and electric field strength $\mathcal{E} = 0.1$ V nm $^{-1}$. The end state is almost purely 1P. **b.** $\mathcal{W} = 200$ fs and $\mathcal{E} = 0.1012$ V nm $^{-1}$. The end state is almost purely 1S. **c.** $\mathcal{W} = 200$ fs and $\mathcal{E} = 0.0085$ V nm $^{-1}$. The end state is fine-tuned to be an equal superposition of 1S and 1P states. Also shown is the population leakage to all other (discrete or continuum) states. **d.** Versatile bubble dynamics versus different end electron states after the laser pulses. On the left, the bubble evolves into a fissioned state and goes back to the original state in picoseconds. On the right, the bubble evolves into a prolate shape and can stay for microseconds before spontaneous emission happens. In the middle, the bubble remains spherical.

Vacuum Rabi oscillations

We now investigate strong coupling [33, 39–41] between a single electron in the bubble and zero or one photon in a cavity, on resonance at a mid-IR wavelength [42, 43]. In view of the necessary helium environment to hold the electron bubble, the most realistic design for experiments is an on-chip slot waveguide cavity [44], as illustrated in Fig. 4a. The slot serves as both a nanofluidic channel and a photon-confinement channel [45]. The electron can be injected into He-4 by a field emission tip [17, 38] and be carried into the slot by the superfluid, which feels zero resistance in arbitrarily small channels. The pressure can be initially set at 25 bar, slightly below the liquid-solid phase transition, for efficient electron loading. Afterwards, the pressure can be slightly increased to transform the liquid into solid, which freezes the electron in place. An ideal choice of materials for mid-IR slot waveguides are germanium (Ge) on zinc selenide

(ZnSe) (see Methods). Figure 4a shows the simulated field intensity distribution around two Ge rectangular waveguides of dimensions 1 μm high and 1.5 μm wide with a 100 nm slot filled with helium. Photons are dominantly concentrated in the slot. To form a 3D cavity, the waveguide length is cutoff at half of the propagation wavelength.

The eigenstates of a two-level electron coupled with a cavity of fixed number of photons are the well-known dressed states [33, 39]. If the photon number is 0 when the electron is in the excited state, and 1 when the electron is in the ground state, then the eigenstates are vacuum dressed states, which read

$$|+; 0\rangle = \frac{1}{\sqrt{2}}(|1P\rangle \otimes |0\rangle + |1S\rangle \otimes |1\rangle), \quad (3)$$

$$|-; 0\rangle = \frac{1}{\sqrt{2}}(|1P\rangle \otimes |0\rangle - |1S\rangle \otimes |1\rangle), \quad (4)$$

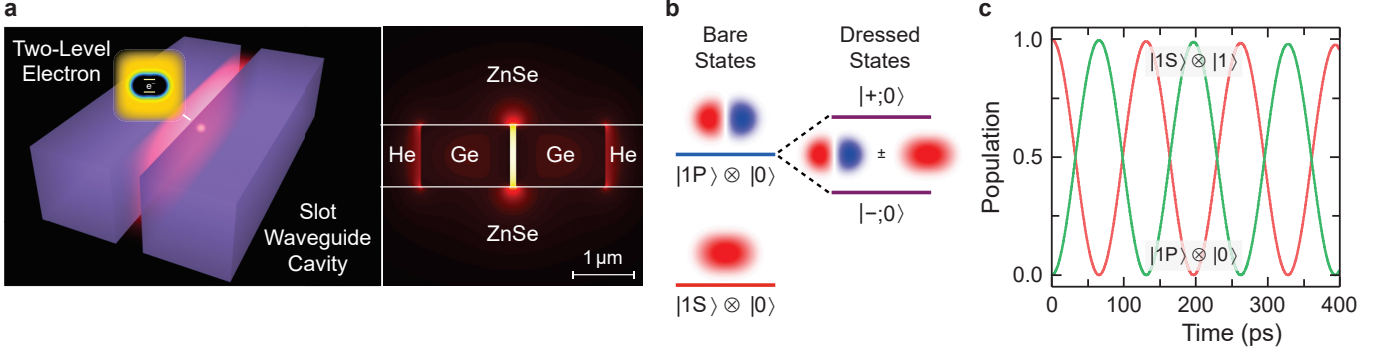


Fig. 4. Strong coupling and vacuum Rabi oscillations of a prolate electron bubble in a slot waveguide cavity. **a.** 3D structure of a slot waveguide cavity: Ge slot waveguide of $1\ \mu\text{m}$ high with $100\ \text{nm}$ slot clamped in ZnSe substrate, and calculated cross-sectional view of the electric field intensity in the cavity on-resonance with the 1S-to-1P transition wavelength. **b.** Formation of the true eigenstates, vacuum dressed states, by equal superpositions of the bare prolate 1S and 1P electron states. **c.** Calculated vacuum Rabi oscillations between the non-eigenstates 1S (photon-in-cavity) and 1P (photon-in-bubble) in a deformed electron bubble coupled with a single cavity photon. The initial state is the prolate 1P state with 0 photon in the cavity.

for on-resonance coupling. Fig. 4b shows the relation between these states. The Rabi-split eigenenergies are $E_{\pm} = \frac{1}{2}\hbar(\omega_{1P} - \omega_{1S}) \pm \frac{1}{2}\hbar\Omega$, in which $\Omega = \sqrt{(\omega_{1P} - \omega_{1S})^2 + 4g^2}$ is the generalized vacuum Rabi frequency [33, 39], $g = d \cdot \mathcal{E}(\mathbf{r}_0)/\hbar$ is the coupling frequency appearing in the Jaynes-Cummings Hamiltonian, d is the transition dipole moment, and $\mathcal{E}(\mathbf{r}_0)$ is the electric field strength of a single-photon wavefunction at the location \mathbf{r}_0 [44]. $|0\rangle$ and $|1\rangle$ in Eqs. (3) and (4) denote the 0- and 1-photon states in the cavity. The electron part suggests that the electron equally popularizes the 1S and 1P states, the same as the equal superposition state in Fig. 3c. The bubble shape of these dressed states is thus the longlived prolate spheroid.

The prolate 1S and 1P electron states (bare states) have the eigenenergies $0.249\ \text{eV}$ and $0.374\ \text{eV}$ from our DFT calculation. The 1S-to-1P transition energy is $0.125\ \text{eV}$, corresponding to a transition wavelength $\lambda = 9.9\ \mu\text{m}$. The calculated transition dipole moment between the prolate 1S and 1P states is $0.544\ \text{e} \cdot \text{nm}$. Our electrodynamic calculation for our slot waveguide design gives a coupling strength $g = 2\pi \times 3.81\ \text{GHz}$ at the field maximum. Comparatively, the spontaneous radiative decay of this two-level electron is $\gamma_r = 0.22\ \text{MHz}$, *i.e.*, $\tau_r = 4.5\ \mu\text{s}$. The intrinsic nonradiative decay in the solid He-4 matrix is $\gamma_{nr} \approx 0.1\ \text{GHz}$, *i.e.*, $\tau_{nr} \approx 10\ \text{ns}$ (10^3 slower than in the liquid [25]). The cavity photon loss rate is $\kappa \approx 0.02\ \text{GHz}$, *i.e.*, a quality factor $Q \approx 4.4 \times 10^6$.

Since in this system $g \gg \gamma_{nr} > \kappa > \gamma_r$, the system is in the electron-photon strong coupling regime. The cooperativity $C = 2g^2/(\kappa\gamma_{nr}) \sim 6 \times 10^5$ is extremely high [46, 47]. If we initialize the system on the non-eigenstates, either the “photon-in-bubble” state $|1P\rangle \otimes |0\rangle$ or the “photon-in-cavity” state $|1S\rangle \otimes |1\rangle$, we can observe longstanding population oscillations, called the vacuum Rabi oscillations (or Rabi flopping), as a result

of the beating between two dressed eigenstates. In Fig. 4c, we can indeed see many cycles of vacuum Rabi oscillations with almost indiscernible damping in hundreds of picoseconds.

Two-electron entanglement

When two electrons are put at the locations \mathbf{r}_a and \mathbf{r}_b in the same cavity, a single photon can be shared by both electrons. The states of interest can be written as the symmetric and antisymmetric entangled states, $|\text{SE}\rangle$ and $|\text{AE}\rangle$, between the two electrons,

$$|\text{SE}\rangle = \frac{1}{\sqrt{2}} (|1S\rangle_{\alpha}|1P\rangle_{\beta} \otimes |0\rangle + |1P\rangle_{\alpha}|1S\rangle_{\beta} \otimes |0\rangle), \quad (5)$$

$$|\text{AE}\rangle = \frac{1}{\sqrt{2}} (|1S\rangle_{\alpha}|1P\rangle_{\beta} \otimes |0\rangle - |1P\rangle_{\alpha}|1S\rangle_{\beta} \otimes |0\rangle). \quad (6)$$

The $|1S\rangle_{\alpha}|1P\rangle_{\beta} \otimes |0\rangle$ and $|1P\rangle_{\alpha}|1S\rangle_{\beta} \otimes |0\rangle$ states represent one photon absorbed in one electron bubble at α or β , and no photon left in the cavity. They can be written as an equal superposition of $|\text{SE}\rangle$ and $|\text{AE}\rangle$. It has been shown [48] that the $|\text{SE}\rangle$ state is a bright state, which is strongly coupled to the cavity, and the $|\text{AE}\rangle$ state is a dark state, which is nearly uncoupled to the cavity. We now demonstrate how a lossy cavity helps to efficiently build up the entanglement between two electrons in a dark state, similar to other dissipation-driven entangled systems [48–50]. Such dissipative production and stabilization protocols have been demonstrated in trapped ion [51] and superconducting qubits [52].

Figure 5a shows the quantum dynamics of entangled states when two electron bubbles are equally coupled, with $g = 2\pi \times 3.81\ \text{GHz}$, to a single cavity photon, starting from the $|1P\rangle_{\alpha}|1S\rangle_{\beta} \otimes |0\rangle$ state. The intrinsic nonradiative decay is taken to be $\gamma_{nr} = 0.1\ \text{GHz}$, the same as above. The upper panel adopts a high-Q cavity with $\kappa = 0.02\ \text{GHz}$. Since the dark state is a natural

eigenstate of the system, uncoupled from the cavity, it maintains a nearly constant population of 0.5. The bright state, on the other hand, oscillates between 0.5 and 0, coupling into the cavity mode. The initial state is completely unentangled, having a concurrence [53] of 0. As the bright state oscillates into the cavity, the concurrence grows, reaching a maximum when the bright state reaches a population of 0. The lower panel adopts a low-Q (highly-lossy) cavity $\kappa = 10$ GHz. In this case, the bright state oscillations are quickly damped out, leaving a long-lived entangled state from the remaining dark state.

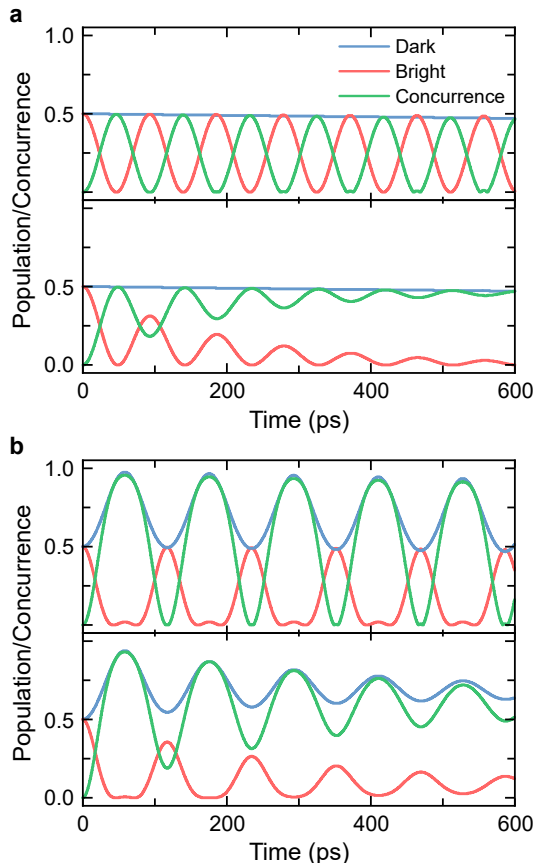


Fig. 5. Evolution of entanglement between two prolate electron bubbles strongly coupled with a single photon in a slot-waveguide cavity. The photon frequency is on resonance with the 1S-to-1P transition. The initial state is a one-electron 1P state. Population of the (bright) symmetric entangled state, the (dark) antisymmetric entangled state, and the concurrence are plotted as a function of time. **a.** Evenly coupled electrons with $\kappa = 0.02$ GHz (upper panel) or 10 GHz (lower panel) cavity photon loss rate. **b.** Unevenly coupled electrons with $\kappa = 0.02$ GHz (upper panel) or 10 GHz (lower panel) cavity photon loss rate.

If we allow the two electron bubbles to have different couplings to the cavity, typically by locating them at different points in the cavity, the amount of entanglement can be enhanced. Fig. 5b shows the dynamics when the initially excited electron bubble has half the coupling strength as the other electron bubble. The dark state

is now weakly coupled into the cavity mode. This causes an indirect coupling between the bright and dark states through the cavity, eventually leading to a large gain in the antisymmetric population. The upper panel of Fig. 5b shows that the concurrence can reach nearly 1, meaning maximally entangled, when the photon loss rate is low. Increasing the photon loss in the cavity, as shown in the lower panel, causes the oscillations to damp out quickly, but the final concurrence goes to 0.6, higher than the case when the two bubbles are equally coupled. This photon-dissipation driven entanglement is not limited to two bubbles; if more were coupled into the cavity, they would also become entangled in a genuine multipartite way, where every electron bubble shares some degree of bipartite entanglement with every other electron bubble [50]. This type of entanglement is similar to the W state of quantum information [54]. The entangled states could form the basis of interesting quantum information technologies, such as highly-sensitive quantum sensors or generators of cluster states for measurement-based quantum computing [55, 56]. Proposals for measuring such entanglement include looking at the bunching and anti-bunching statistics of the system's emitted photons [57, 58].

Conclusion

We have proposed a unique system of single electrons in condensed helium-4 as a new platform of quantum nodes in a quantum network. A single electron in helium can be coherently manipulated by mid-IR photons in both the strong-pulse regime and single-photon regime, and exhibit driven and vacuum Rabi oscillations. Two electrons can form entangled states through natural coupling with an optical cavity and show nanoseconds lifetime. Combined with the single-electron state control via laser pulses and the long lifetimes of the entangled states, the electron-in-helium system offers an attractive avenue for quantum information science and technology.

Methods

Density functional calculation

We calculate the electronic structure in condensed He-4 using a density-functional formalism [19, 28], which is a generalization to the Gross-Pitaevskii equation formalism in the Bose-Einstein condensation (BEC) systems [26]. Our density-functional formalism can accurately reproduce most properties of He-4 at near zero temperature, including: a. the equation of states and surface tension [59, 60]; b. the 1 eV potential barrier of helium to electron at zero pressure [27]; c. real-time vortex nucleation and sound emission [28, 34].

The energy functional of the combined electron-in-helium system is written as

$$\begin{aligned}
 E[\psi, \varphi] = & \int d\mathbf{r} \frac{\hbar^2}{2m_{\text{He}}} |\nabla\psi|^2 + \frac{\hbar^2}{2m_e} |\nabla\varphi|^2 \\
 & + \frac{1}{2}g_2|\psi|^4 + \frac{1}{3}g_3|\psi|^6 + \frac{1}{4}g_4|\psi|^8 \\
 & + \frac{1}{2}w|\nabla|\psi|^2|^2 + f_0|\varphi|^2|\psi|^2,
 \end{aligned} \tag{7}$$

where ψ is the macroscopic wavefunction of helium normalized to the number N of helium atoms, and φ is the wavefunction of a single electron. This functional encloses the two-particle, three-particle, and four-particle correlations between helium atoms through the g_2, g_3, g_4 terms and the surface energy through the h_2 term [59, 60]. It approximates the electron-helium interaction at the s-wave scattering level by the $f_0 = 2\pi\hbar^2 l/m_e$ term [27].

The equations of motion consistent with this functional can be derived as

$$i\hbar\partial_t\psi = -\frac{\hbar^2}{2m_{\text{He}}}\nabla^2\psi + (g_2|\psi|^2 + g_3|\psi|^6 + g_4|\psi|^8)\psi - h_2\nabla(|\psi|^2)\psi + f_0|\varphi|^2\psi - \mu\psi, \quad (8)$$

$$i\hbar\partial_t\varphi = -\frac{\hbar^2}{2m_e}\nabla^2\varphi + f_0|\psi|^2\varphi, \quad (9)$$

where μ is the chemical potential which varies with pressure. These two coupled equations are highly nonlinear. Numerically evolving these equations in real or imaginary time (with a paralleled 4th-order finite-difference and 4th-order Runge-Kutta scheme) can exhibit remarkable quantum nonequilibrium and equilibrium behaviors [19, 28].

Master equation calculation

We calculate the quantum optical dynamics using the Lindblad master equation,

$$\frac{d\rho}{dt} = -i[H, \rho] + L(\rho), \quad (10)$$

where ρ is the density matrix of the system, H is the system Hamiltonian, possibly including time-dependent terms, and $L(\rho)$ are the Lindblad superoperators describing dissipation and decay.

For the laser driven Rabi oscillations of Fig. 3a-c, the Hamiltonian, H , is defined by diagonal matrix elements, H_0 , which represent the energy of each state ($|1S\rangle\langle 1S|$ type terms) and off-diagonal matrix elements, H_1 , which represent the dipole moment between two states ($|1S\rangle\langle 1P| + |1P\rangle\langle 1S|$ type terms). 48 states were included in the Hamiltonian, approximating the infinite continuum. The values of the matrix elements were computed using the density functional approach described above. The total Hamiltonian was $H = H_0 + E(t)H_1$, where $E(t) = G(t)\mathcal{E}\cos(\omega_0 t)$, $G(t)$ is a Gaussian envelope such that the full width at half maximum of $E^2(t)$ is the pulse length, \mathcal{W} , and the pulse strength is \mathcal{E} . The pulse frequency, ω_0 , was on resonance with the $|1S\rangle$ to $|1P\rangle$ transition. Various pulse strengths (\mathcal{E}) and pulse lengths (\mathcal{W}) were used. Because of the strong laser driving in part of our studies, our calculation generally does not presume the rotating wave approximation (RWA). Hence our Rabi oscillations results may display high-frequency oscillations on top. Due to the long radiative and non-radiative lifetimes, no Lindblad terms were included in the simulations for Fig. 3a-c. The simulation for Fig. 6a used the same Hamiltonian but the frequency, ω_0 , was on resonance with half the $|1S\rangle$ to $|2S\rangle$ transition frequency.

For the vacuum driven Rabi oscillations of Fig. 4c, the Hamiltonian describing the states of the electron bubble was truncated to include just the $|1S\rangle$ and $|1P\rangle$ states and a cavity, also truncated to two states, was added. The resulting Hamiltonian was, then,

$$H = \omega_{1S\rightarrow 1P}|1P\rangle\langle 1P| + \omega_{1S\rightarrow 1P}a^\dagger a + g(|1S\rangle\langle 1P| + |1P\rangle\langle 1S|)(a + a^\dagger), \quad (11)$$

where $\omega_{1S\rightarrow 1P}$ is the $|1S\rangle$ to $|1P\rangle$ transition frequency, a is the annihilation operator for the cavity, and g is the electron bubble-cavity coupling of the slot waveguide design described in Fig. 4a. Spontaneous emission of the two-level electron system was included via a Lindblad term, $L_{e^-}(\rho) = \gamma_r\mathcal{D}[|1P\rangle\langle 1S|](\rho)$, where $\mathcal{D}[C]\rho = C\rho C^\dagger - \frac{1}{2}(C^\dagger C\rho + \rho C^\dagger C)$. Cavity photon loss was included via Lindblad term $L_c(\rho) = \kappa\mathcal{D}[a](\rho)$. Non-radiative decay, which is on the order of nanoseconds, was not included due to its long time scale. The system was initialized in the $|1S\rangle \otimes |1\rangle$ state, representing one photon in the cavity.

For the entanglement generation of Fig. 5, an additional two-level electron bubble was added to the system. The resulting Hamiltonian was

$$H = \omega_{1S\rightarrow 1P}|1P\rangle_{\alpha\alpha}\langle 1P| + \omega_{1S\rightarrow 1P}|1P\rangle_{\beta\beta}\langle 1P| + \omega_{1S\rightarrow 1P}a^\dagger a + g_\alpha(|1S\rangle_{\alpha\alpha}\langle 1P| + |1P\rangle_{\alpha\alpha}\langle 1S|)(a + a^\dagger) + g_\beta(|1S\rangle_{\beta\beta}\langle 1P| + |1P\rangle_{\beta\beta}\langle 1S|)(a + a^\dagger), \quad (12)$$

where the subscripts α and β represent the different electron bubbles. In this Hamiltonian, each bubble is coupled to the cavity (potentially with different strengths) but the bubbles are not coupled to each other. Spontaneous emission was included for each electron bubble using $L_{\alpha,r} = \gamma_r\mathcal{D}[|1P\rangle_{\alpha\alpha}\langle 1S|](\rho)$ and $L_{\beta,r} = \gamma_r\mathcal{D}[|1P\rangle_{\beta\beta}\langle 1S|](\rho)$. Non-radiative emission was included via $L_{\alpha,nr} = \gamma_{nr}\mathcal{D}[|1P\rangle_{\alpha\alpha}\langle 1S|](\rho)$ and $L_{\beta,nr} = \gamma_{nr}\mathcal{D}[|1P\rangle_{\beta\beta}\langle 1S|](\rho)$. Cavity loss was also included (see above).

Material choice for mid-IR slot waveguides

Ga and ZnSe both are widely transparent in the 1 to 12 μm wavelength range [61, 62] and have almost perfectly matched lattice constant (5.658 \AA versus 5.668 \AA) [63], which is superior for molecule beam epitaxy (MBE) growth and wafer bonding process. Furthermore, ZnSe is transparent in the visible wavelength down to 600 nm wavelength, particularly convenient for optical alignment. Compared with vacuum ($\epsilon_{\text{vac}} = 1$) and helium ($\epsilon_{\text{He}} = 1.057$), both materials have a large dielectric contrast ($\epsilon_{\text{Ge}} = 15.5$ and $\epsilon_{\text{ZnSe}} = 5.76$), especially good for on-chip light confinement. To experimentally realize the slot waveguide structure shown in the main text, one can use photolithography and dry etching to first produce a 3 μm wide ridge on the substrate, and then use a focused ion beam (FIB) to make a 100 nm wide 1 μm deep slot in the middle. Photons can be sent into the cavity by direct illumination on top of the chip.

Scheme of two-photon fluorescence imaging

In practice, to precisely locate and optically manipulate a single electron in condensed helium, we need to develop a confocal microscopy based on a certain fluorescence channel, similar to the technique used for defect centers in diamond [64].

The 1-photon $1S$ -to- $1P$ transition shown in Fig. 3 is not an ideal fluorescence channel either in liquid or solid helium. The complex shape deformation and phonon emission sensitively depend on the laser pulse width and strength, and can cause completely quenched or overly broadened fluorescence spectrum. Instead, the 2-photon $1S$ -to- $2S$ transition is a better channel for imaging. As sketched in the inset of Fig. 2, the electron first jumps into a virtual level between the $1S$ and $2S$ state [39] and then into the $2S$ state, by sequentially absorbing two photons at the frequency $\omega = (\omega_{2S} - \omega_{1S})/2$.

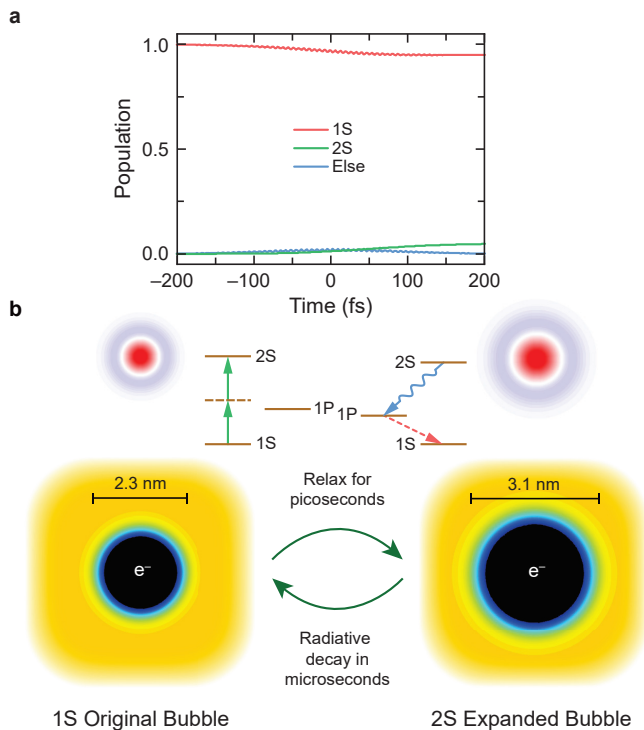


Fig. 6. Two-photon transition from the 1S to 2S state for a spherical bubble under 25 bar pressure and the fluorescence and bubble dynamics after the laser pulse. (a) Population of the 1S and 2S states for the pulse width $\mathcal{W} = 200$ fs and electric field strength $\mathcal{E} = 0.05$ V nm $^{-1}$. (c) Processes of isotropic expansion of the 2S bubble state after the excitation, the 2S-to-1P radiative decay and then nonradiative relaxation back to 1S bubble.

Afterwards, the electron makes a 1-photon 2S-to-1P transition by the spontaneous emission and produces a fluorescence photon at a fixed wavelength.

For most systems under conventional laser illumination, the 2-photon transition rate is low [39]. However, we find that the pulse energy from a parametrically amplified femtosecond laser provides a decent probability to bring the electron into the 2S state. The 2-photon transition wavelength at $p = 25$ bar pressure from our calculation is $\lambda = 4.08$ μm . As shown in Fig. 6a, after a single laser pulse of $W = 200$ fs and $\mathcal{E} = 0.05$ V nm $^{-1}$, the electron has about 5% population on the 2S state. There is little leakage to other states (mainly the nearby 1P state). This transition rate is sufficient to give strong signal on a mid-IR photodetector [65].

Interestingly, before the 2S-to-1P radiative decay sets in, the 2S bubble has to undergo a nonradiative isotropic expansion first, as illustrated in Fig. 6c [66]. This is due to the increased quantum pressure of 2S electron wavefunction exerted on the bubble surface. Our calculation shows that the bubble radius increases from 1.14 nm to 1.54 nm in a time scale about 10 ps. The final 2S state is metastable and does not exhibit further deformation or nonradiative decay. It decays only through the spontaneous emission into the 1P state in the expanded bubble. The 1-photon fluorescence wavelength for the expanded 2S to 1P state is $\lambda = 5.13$ μm , and the dipole moment is $d = 0.31$ e-nm. The spontaneous emission rate can be calculated to be $\gamma = 5.20 \times 10^5$ s $^{-1}$,

i.e., lifetime $\tau = 1.92$ μs . After the 2S-to-1P transition, the bubble will likely undergo a similar fission process as Fig. 3a, and finally relax back to the original 1S ground state. This final nonradiative relaxation from the 1P state back to 1S state has no impact on the already emitted photon. Hence the 2-photon 1S-to-2S transition provides a reliable approach for confocal imaging single electrons in condensed helium.

Data availability

All relevant data are available from the authors on request.

Code availability

All relevant codes are available from the authors on request.

Acknowledgments

This work was performed at the Center for Nanoscale Materials, a U.S. Department of Energy Office of Science User Facility, and supported by the U.S. Department of Energy, Office of Science, under Contract No. DE-AC02-06CH11357.

* djin@anl.gov

- [1] H. J. Kimble, *Nature* **453**, 1023 (2008).
- [2] S. Tanzilli, W. Tittel, M. Halder, O. Alibart, P. Baldi, N. Gisin, and H. Zbinden, *Nature* **437**, 116 (2005).
- [3] J. L. O'brien, A. Furusawa, and J. Vučković, *Nat. Photon.* **3**, 687 (2009).
- [4] J. Weber, W. Koehl, J. Varley, A. Janotti, B. Buckley, C. Van de Walle, and D. D. Awschalom, *Proc. Natl. Acad. Sci.* **107**, 8513 (2010).
- [5] K. De Greve, L. Yu, P. L. McMahon, J. S. Pelc, C. M. Natarajan, N. Y. Kim, E. Abe, S. Maier, C. Schneider, M. Kamp, *et al.*, *Nature* **491**, 421 (2012).
- [6] S. Thiele, F. Balestro, R. Ballou, S. Klyatskaya, M. Ruben, and W. Wernsdorfer, *Science* **344**, 1135 (2014).
- [7] J. T. Muhonen, J. P. Dehollain, A. Laucht, F. E. Hudson, R. Kalra, T. Sekiguchi, K. M. Itoh, D. N. Jamieson, J. C. McCallum, A. S. Dzurak, *et al.*, *Nat. Nano.* **9**, 986 (2014).
- [8] M. Saffman, *J. Phys. B: Atomic, Molecular and Opt. Phys.* **49**, 202001 (2016).
- [9] K. R. Brown, J. Kim, and C. Monroe, *npj Quantum Information* **2**, 16034 (2016).
- [10] F. H. Koppens, C. Buizert, K.-J. Tielrooij, I. T. Vink, K. C. Nowack, T. Meunier, L. Kouwenhoven, and L. Vandersypen, *Nature* **442**, 766 (2006).
- [11] X. Mi, J. Cady, D. Zajac, P. Deelman, and J. Petta, *Science* **355**, 156 (2017).
- [12] W. Sommer, *Phys. Rev. Lett.* **12**, 271 (1964).
- [13] M. H. Cohen and J. Jortner, *Phys. Rev.* **180**, 238 (1969).
- [14] P. Moroshkin, A. Hofer, and A. Weis, *Phys. Rep.* **469**, 1 (2008).
- [15] G. Sabouret, F. Bradbury, S. Shankar, J. Bert, and S. A. Lyon, *Appl. Phys. Lett.* **92**, 082104 (2008).
- [16] C. Grimes and G. Adams, *Phys. Rev. B* **45**, 2305 (1992).
- [17] A. I. Golov and L. P. Mezhov-Deglin, *Physica B: Cond. Matt.* **194**, 951 (1994).
- [18] H. Maris, *J. Low Temp. Phys.* **132**, 77 (2003).
- [19] D. Jin, W. Guo, W. Wei, and H. Maris, *J. Low Temp. Phys.* **158**, 307 (2010).
- [20] A. J. Leggett, S. Chakravarty, A. T. Dorsey, M. P. Fisher, A. Garg, and W. Zwerger, *Rev. Mod. Phys.* **59**, 1 (1987).

- [21] J. Wilks, *The properties of liquid and solid helium* (Clarendon Press, 1967).
- [22] A. J. Leggett *et al.*, *Quantum liquids: Bose condensation and Cooper pairing in condensed-matter systems* (Oxford university press, 2006).
- [23] F. Werner, G. Beaume, A. Hobeika, S. Nascimbene, C. Herrmann, F. Caupin, and S. Balibar, *J. Low. Temp. Phys.* **136**, 93 (2004).
- [24] V. Dionne, R. Young, and C. Tomizuka, *Phys. Rev. A* **5**, 1403 (1972).
- [25] V. B. Shikin, *Sov. Phys. Uspekhi* **20**, 226 (1977).
- [26] N. G. Berloff and P. H. Roberts, *Phys. Rev. B* **63**, 024510 (2000).
- [27] V. Grau, M. Barranco, R. Mayol, and M. Pi, *Phys. Rev. B* **73**, 064502 (2006).
- [28] D. Jin and W. Guo, *Phys. Rev. B* **82**, 094524 (2010).
- [29] D. J. Griffiths and D. F. Schroeter, *Introduction to quantum mechanics* (Cambridge University Press, 2018).
- [30] With the laser field strength used in our paper, we have calculated and confirmed that the probabilities for single- or multi-photon transitions onto other localized or continuum states are all order-of-magnitude smaller than the presented transitions.
- [31] D. Konstantinov and H. J. Maris, *Phys. Rev. Lett.* **90**, 025302 (2003).
- [32] Spectra-Physics, *Data sheets of femtosecond lasers and optical parametric amplifiers: <https://www.spectra-physics.com/products/ultrafast-lasers/topas>* (Newport Corp., 2019).
- [33] M. O. Scully and M. S. Zubairy, *Quantum optics* (AAPT, 1999).
- [34] D. Mateo, D. Jin, M. Barranco, and M. Pi, *J. Chem. Phys.* **134**, 044507 (2011).
- [35] H. J. Maris, *J. Low Temp. Phys.* **120**, 173 (2000).
- [36] R. Jackiw, C. Rebbi, and J. Schrieffer, *J. Low Temp. Phys.* **122**, 587 (2001).
- [37] J. L. Flowers and B. W. Petley, *Reports on Progress in Physics* **64**, 1191 (2001).
- [38] W. Wei, Z. Xie, L. N. Cooper, and H. J. Maris, *J. Low Temp. Phys.* **185**, 313 (2016).
- [39] R. W. Boyd, *Nonlinear optics* (Elsevier, 2003).
- [40] H. J. Kimble, *Physica Scripta* **1998**, 127 (1998).
- [41] A. Boca, R. Miller, K. Birnbaum, A. Boozer, J. McKeever, and H. Kimble, *Phys. Rev. Lett.* **93**, 233603 (2004).
- [42] R. Soref, *Nature photonics* **4**, 495 (2010).
- [43] Y. Chen, H. Lin, J. Hu, and M. Li, *ACS Nano* **8**, 6955 (2014).
- [44] M. P. Hiscocks, C.-H. Su, B. C. Gibson, A. D. Greentree, L. C. Hollenberg, and F. Ladouceur, *Opt. Express* **17**, 7295 (2009).
- [45] A. Duh, A. Suhel, B. Hauer, R. Saeedi, P. Kim, T. Biswas, and J. Davis, *J. Low Temp. Phys.* **168**, 31 (2012).
- [46] L. Greuter, S. Starosielec, A. V. Kuhlmann, and R. J. Warburton, *Phys. Rev. B* **92**, 045302 (2015).
- [47] D. Dovzhenko, S. Ryabchuk, Y. P. Rakovich, and I. Nabiev, *Nanoscale* **10**, 3589 (2018).
- [48] M. Otten, R. A. Shah, N. F. Scherer, M. Min, M. Pelton, and S. K. Gray, *Phys. Rev. B* **92**, 125432 (2015).
- [49] D. Martin-Cano, A. Gonzalez-Tudela, L. Martin-Moreno, F. J. Garcia-Vidal, C. Tejedor, and E. Moreno, *Phys. Rev. B* **84**, 235306 (2011).
- [50] M. Otten, J. Larson, M. Min, S. M. Wild, M. Pelton, and S. K. Gray, *Phys. Rev. A* **94**, 022312 (2016).
- [51] Y. Lin, J. Gaebler, F. Reiter, T. R. Tan, R. Bowler, A. Sørensen, D. Leibfried, and D. J. Wineland, *Nature* **504**, 415 (2013).
- [52] S. Shankar, M. Hatridge, Z. Leghtas, K. Sliwa, A. Narla, U. Vool, S. M. Girvin, L. Frunzio, M. Mirrahimi, and M. H. Devoret, *Nature* **504**, 419 (2013).
- [53] W. K. Wootters, *Phys. Rev. Lett.* **80**, 2245 (1998).
- [54] W. Dür, G. Vidal, and J. I. Cirac, *Phys. Rev. A* **62**, 062314 (2000).
- [55] H. J. Briegel and R. Raussendorf, *Phys. Rev. Lett.* **86**, 910 (2001).
- [56] B. A. Bell, M. S. Tame, A. S. Clark, R. W. Nock, W. J. Wadsworth, and J. G. Rarity, *New. J. Phys.* **15**, 053030 (2013).
- [57] M. Otten, S. Gray, and G. Kolmakov, *Phys. Rev. A* **99**, 032339 (2019).
- [58] E. Dumitrescu and B. Lawrie, *Physical Review A* **96**, 053826 (2017).
- [59] F. Dalfovo, A. Lastrì, L. Pricaupeko, S. Stringari, and J. Treiner, *Phys. Rev. B* **52**, 1193 (1995).
- [60] S. Stringari and J. Treiner, *Phys. Rev. B* **36**, 8369 (1987).
- [61] S. Kim, J.-H. Han, J.-P. Shim, H.-j. Kim, and W. J. Choi, *Opt. Mater. Express* **8**, 440 (2018).
- [62] J. R. Macdonald, S. J. Beecher, P. A. Berry, G. Brown, K. L. Schepler, and A. K. Kar, *Opt. Lett.* **38**, 2194 (2013).
- [63] J. Calow, S. Owen, and P. Webb, *physica status solidi (b)* **28**, 295 (1968).
- [64] A. Gruber, A. Dräbenstedt, C. Tietz, L. Fleury, J. Wrachtrup, and C. Von Borczyskowski, *Science* **276**, 2012 (1997).
- [65] P. Norton, *Opt. Rev.* , 159 (2002).
- [66] Several authors adopted a sharp-wall infinite-barrier model to calculate the stability of 2S bubble and found that it evolves into a tetrahedra shape [67, 68]. However, we have performed a more accurate 3D DFT calculation, and found no indication of such symmetry breaking.
- [67] H. J. Maris and W. Guo, *J. Low Temp. Phys.* **148**, 207 (2007).
- [68] P. Grinfeld and H. Kojima, *Phys. Rev. Lett.* **91**, 105301 (2003).